



Hierarchical $\text{MoS}_2/\text{Bi}_2\text{MoO}_6$ composites with synergistic effect for enhanced visible photocatalytic activity

Yajie Chen^a, Guohui Tian^{a,b,*}, Yunhan Shi^a, Yuting Xiao^a, Honggang Fu^{a,**}

^a Key Laboratory of Functional Inorganic Material Chemistry, Ministry of Education of the People's Republic of China, Heilongjiang University, Harbin 150080 PR China

^b Key Laboratory of Chemical Engineering Process & Technology for High-efficiency Conversion, College of Heilongjiang Province, School of Chemistry and Materials Science, Heilongjiang University, Harbin 150080, China

ARTICLE INFO

Article history:

Received 16 June 2014

Received in revised form 19 August 2014

Accepted 21 August 2014

Available online 28 August 2014

Keywords:

$\text{MoS}_2/\text{Bi}_2\text{MoO}_6$

In situ growth

Heterostructure

Visible light

Active radicals

ABSTRACT

Compared with the conventional solution deposition methods used for the synthesis of composites, in situ controlled growth was employed to construct hierarchical $\text{MoS}_2/\text{Bi}_2\text{MoO}_6$ composites with enhanced photocatalytic activity. In the reaction process, the preexfoliated layered MoS_2 nanoslices acted as an excellent supporting matrix for the in situ growth of Bi_2MoO_6 nanoflakes, which in return inhibited the photocorrosion of MoS_2 nanoslices. The obtained hierarchical $\text{MoS}_2/\text{Bi}_2\text{MoO}_6$ composites exhibited significantly enhanced performance for photocatalytic oxidation of Rhodamine B compared with pure Bi_2MoO_6 under visible light irradiation due to the improved photogenerated charge separation, boosted catalytic active sites and light harvesting. To evaluate the photocatalytic system, the degradation process of Rhodamine B was also investigated. The active species trapping and control experiments indicated that the formed junctions between Bi_2MoO_6 and MoS_2 improved charge transfer property, which was proved by the surface photovoltage spectroscopy, photoluminescence and electrochemical impedance measurements.

© 2014 Elsevier B.V. All rights reserved.

1. Introduction

Over the past decades, heterogeneous photocatalysis has been considered as a promising process for environmental purification [1,2]. Extensive efforts have been devoted to the development of highly efficient photocatalysts. In general, the efficient photocatalysts are usually wide-gap semiconductors, which can only utilize UV light irradiation [3,4]. From the viewpoint of solar energy utilization, the development of visible-light driven photocatalyst is indispensable [5]. However, most of the visible light photocatalysts possesses relatively low photocatalytic activity. In practice, the achievement of high photocatalytic performance necessitates the spatial integration of semiconductors and co-catalysts to form surface junctions, so as to optimize the capture of light and allow

the prompt migration of light-induced charge, thus resulting in an efficient photocatalytic reaction.

Recently, studies on compositions constructed by two dimensional (2D) nanosheets with zero-dimensional (0D) nanoparticles or one-dimensional (1D) nanowires have been extensively carried out to improve the performance and the application scope of the materials [6,7]. Especially, 2D graphene and graphitic carbon nitride (g-CN) nanosheets were often used as supporters to construct the heterojunctional composite photocatalysts with high photocatalytic activity via different strategies, such as the direct crystal growth of the metal oxide on their surface in an aqueous colloidal suspension [8]. Similarly, MoS_2 , a typical layered transition-metal dichalcogenide family, has also received great attention as a cocatalyst in photocatalytic hydrogen evolution, and the deposition of MoS_2 on the surfaces of the catalysts enhanced the photocatalytic activity [9]. But there also existed some questions in these synthetic methods, such as the increased light blocking effect and the weak interaction between two components in the composites. It greatly inhibited the further enhancement of photocatalytic activity [10]. More recently, single-layer MoS_2 nanosheets were used as substrate to construct the noble metal– MoS_2 hybrid nanomaterials by the in situ growth of noble metal nanoparticles [11]. The prepared noble metal– MoS_2 hybrid nanomaterials exhibited

* Corresponding author at: Key Laboratory of Functional Inorganic Material Chemistry, Ministry of Education of the People's Republic of China, Heilongjiang University, Harbin 150080 P. R. China. Tel.: +86 451 8660 4330; fax: +86 451 8667 3647.

** Corresponding author. Tel.: +86 451 8660 4330; fax: +86 451 8667 3647.

E-mail addresses: tiangh@hlju.edu.cn (G. Tian), honggangfu@126.com (H. Fu).

better electrocatalytic activity than the commercial noble metal catalyst at the same noble metal loading. Inspired by their study, it is expected to construct hierarchical MoS_2 /oxide semiconductor composites with synergistic effect for high performance photocatalytic activity.

Among these semiconductor photocatalysts, bismuth based photocatalysts have been widely studied [12]. Among these bismuth based photocatalysts, Bi_2MoO_6 is thought as an ideal photocatalyst from the viewpoint of using visible light [13]. However, the photocatalytic performance of Bi_2MoO_6 is still far from satisfactory due to the high recombination rate of photogenerated electron–hole pairs [14]. It has been demonstrated that Bi_2MoO_6 -based composites with high performance can be achieved by proper nanostructuring [15]. Inspired by the successful synthesis of many other metal oxide-based heterojunctional composites, Bi_2MoO_6 -based heterojunctional composites with high interfacial charge transfer between two components are highly desirable and anticipated as superior photocatalysts [16].

Herein, we reported a facile method to synthesize hierarchical $\text{MoS}_2/\text{Bi}_2\text{MoO}_6$ composites via a two-step process. The 2D platform structure MoS_2 nanoslices were first exfoliated to act as excellent supporters for the growth of Bi_2MoO_6 nanoflakes, then Bi_2MoO_6 nanoflakes were in situ grown on the surfaces of the exfoliated MoS_2 nanoslices during the solvothermal process. This synthetic method contributed to the formation of junctions between Bi_2MoO_6 and MoS_2 , which can allow the prompt migration of photogenerated charge and reduce the self-agglomeration. The photocatalytic degradation process of Rhodamine B was also investigated.

2. Experimental

2.1. Exfoliation of layered commercial MoS_2 nanoslices

The exfoliation of layered commercial MoS_2 was completed according to the modified report [17]. Sixty milligram commercial MoS_2 powder was added to 20 mL of ethanol/water with EtOH volume fractions of 45% was added as dispersion solvent. The sealed flask was sonicated for 8 h, and then the dispersion was centrifuged at 3000 rpm for 20 min to remove aggregations. Finally, the supernatant (the exfoliated MoS_2 nanoslices) was collected and used to synthesize hierarchical $\text{MoS}_2/\text{Bi}_2\text{MoO}_6$ composites.

2.2. Synthesis of hierarchical $\text{MoS}_2/\text{Bi}_2\text{MoO}_6$ composites

In a typical case, 0.5622 g $\text{Bi}(\text{NO}_3)_3 \cdot 5\text{H}_2\text{O}$ and 0.1403 g $\text{Na}_2\text{MoO}_4 \cdot 2\text{H}_2\text{O}$ were dissolved in 10 mL of ethylene glycol under magnetic stirring. The exfoliated MoS_2 nanoslices (the weight ratios of MoS_2 to Bi_2MoO_6 were 2 wt%, 4 wt%, 6 wt% and 8 wt%) was dispersed into ethanol (20 mL) by ultrasonication for 30 min, respectively. Then it was slowly added into the above solution, followed by stirring for 10 min. The resulting suspension was transferred into a 50 mL teflon-lined stainless steel autoclave. The mixture was then heated to 160 °C and maintained for different reaction times (1, 3, 6 and 10 h). Subsequently, the autoclave was cooled to room temperature naturally. The obtained samples were filtered, washed with ethanol and dried at 80 °C in air. For comparison, the blank Bi_2MoO_6 was prepared in the absence of MoS_2 using the same experimental conditions.

In order to obtain the detail content of Bi_2MoO_6 in the $\text{MoS}_2/\text{Bi}_2\text{MoO}_6$ composites, we added a certain amount of $\text{MoS}_2/\text{Bi}_2\text{MoO}_6$ composites into diluted nitric acid (3 mol L^{-1}) and stirred overnight to ensure that the composite was dissolved completely. Then the clear solution was diluted and determined by ICP-AES (Optima 7000DV) to get the concentration of Bi and Mo

elements, respectively, so the content of Bi_2MoO_6 and MoS_2 in the composite can be calculated, respectively. For the $\text{MoS}_2/\text{Bi}_2\text{MoO}_6$ composites prepared using 2 wt%, 4 wt%, 6 wt% and 8 wt% MoS_2 , the detected MoS_2 content is 2.13 wt%, 4.17 wt%, 6.25 wt% and 8.36 wt%.

2.3. Characterization

Structure and morphology of the product was investigated by scanning electron microscopy (SEM, Hitachi S-4800, Japan), transmission electron microscopy (TEM, JEOL 2100, Japan), and powder X-ray diffraction (XRD, Bruker D8 Advance using CuKa radiation). The UV-visible diffuse reflectance spectra of films were obtained using a UV-visible spectrophotometer (Shimadzu UV-2550). The electronic states of elements in the sample were analyzed using X-ray photoelectron spectroscopy (XPS, Kratos-AXIS UL TRA DLD, Al Ka X-ray source). Photoluminescence (PL) spectra were measured at room temperature using a Fluoromax-4 spectrophotometer (Horiba Jobin Yvon). The electrochemical impedance spectra (EIS) of the thin film made from these as-made materials were measured via a computer-controlled IM6e impedance measurement unit (Zahner Elektrik, Germany) in 0.1 M Na_2S and 0.02 M Na_2SO_3 aqueous solution under UV light and carried out by applying sinusoidal perturbations of 10 mV under bias of -0.8 V , and the frequency ranges from 0.05 to 100 kHz. The excitation wavelength was 300 nm, and the emission slit was 1.0 nm. The surface photovoltage spectra (SPV) were carried out on a laboratory-built surface photovoltage spectroscopy. A 150 W xenon lamp with a monochromator was used as light source. A lock-in amplifier (SR830-DSP, USA) synchronized with a light chopper was employed to amplify the photovoltage signal. The spectral resolution was 1 nm. SPV measurements were carried out with a solid-junction photovoltaic FTO/sample/FTO sandwich structure. The generation of photovoltage arose from the creation of electron hole pairs followed by the separation under a built-in electric field (the space charge layer).

2.4. Measurement of photocatalytic activity

The photocatalytic activities of the catalysts were evaluated by the degradation of Rhodamine B (RhB) under visible light irradiation in a slurry reactor containing 0.1 g of catalyst, 50 mL of RhB solution (10 mg L^{-1}). A 150 W Xe lamp was used as a light source, and a 420 nm cutoff filter was placed above the reactor to cut off the UV light. Prior to irradiation, the suspension was kept in the dark under stirring for 60 min to ensure the establishing of an adsorption/desorption equilibrium. At given time intervals, 2 mL aliquots were collected from the suspension and immediately centrifuged, the concentration of RhB after illumination was determined at 554 nm using a UV-vis spectrophotometer (Shimadzu UV-2550). After the measurement, the sampled RhB solution was returned to the reactor to make sure that the total volume of the reaction solution is unchanged. The de-ethylation intermediates of RhB were determined by an HPLC method. The HPLC system (shimadzu LC-20AT) consisted of a Dionex P580 pump, a UVD 340S Diode Array detector, and an intersil ODS-3 C_{18} reverse column ($5\text{ }\mu\text{m}$, $250 \times 4.6\text{ mm}^2$).

A total organic carbon (TOC) analyzer (AnalytikJena, Multi N/C 2100S, Germany) was employed for mineralization degree analysis of the dye solutions. Prior to injection into the TOC analyzer, the samples were filtrated with a $0.45\text{ }\mu\text{m}$ Millipore filter. All experiments were carried out at least in duplicate. The reported values were within the experimental error range of $\pm 3\%$. To detect the active species generated during photocatalytic reactivity, various scavengers were added into the solution of RhB, including 1.0 mM isopropanol (IPA, a quencher of $\cdot\text{OH}$), 1 mM p-benzoquinone (BQ,

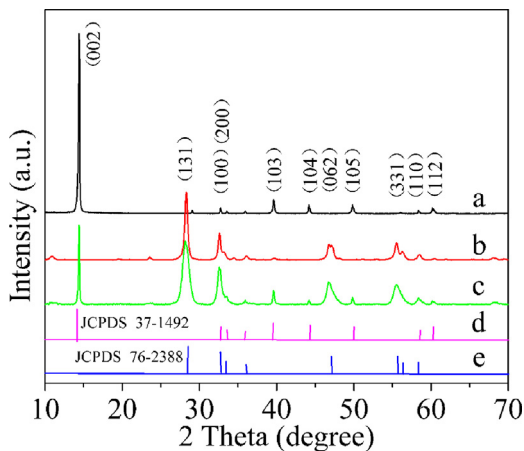


Fig. 1. XRD patterns of MoS₂ (a), Bi₂MoO₆ (b) and the hierarchical MoS₂/Bi₂MoO₆ composite (6 wt% of MoS₂) (c), standard diffraction card of MoS₂ (JCPDS card no. 37-1492) (d), and standard diffraction card of Bi₂MoO₆ (JCPDS card no. 76-2388) (e).

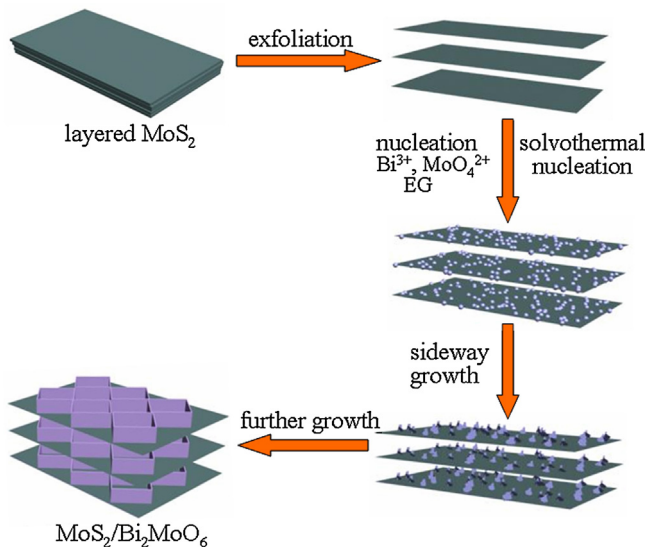
a quencher of O₂^{•-}) or 1 mM triethanolamine (TEOA, a quencher of h⁺), 6 mM AgNO₃ (e⁻ scavenger).

3. Results and discussion

3.1. Crystalline and morphologic properties of the hierarchical MoS₂/Bi₂MoO₆ composites

Fig. 1 shows the X-ray diffraction (XRD) patterns of the obtained samples. It can be found that the pure Bi₂MoO₆ shows the diffraction peaks (curve b in Fig. 1) of (131), (200), (151), (062), (331) and (262) planes at 2θ = 28.3°, 32.9°, 35.9°, 47.1°, 55.9° and 58.5°, which can be indexed to orthorhombic phase of Bi₂MoO₆ (JCPDS card no. 76-2388) [18]. As for the pure MoS₂ (curve a in Fig. 1), the detected XRD pattern peaks at 2θ = 14.5°, 32.7°, 39.7°, 49.8° and 58.4° can be assigned to the (002), (100), (103), (105) and (110) planes in the orthorhombic phase of MoS₂ (JCPDS card no. 37-1492), respectively [19]. In the case of the MoS₂/Bi₂MoO₆ composite, the XRD pattern (curve c of Fig. 1) displays two kinds of diffraction peaks, besides the diffraction peaks assigned to orthorhombic phase of MoS₂, all additional ones are well-matched to the orthorhombic phase Bi₂MoO₆, indicating the presence of Bi₂MoO₆ nanoflakes grown on MoS₂ nanoslices.

The morphology and microstructure of the hierarchical MoS₂/Bi₂MoO₆ composite were observed by SEM and TEM. For comparison, SEM image of the exfoliated MoS₂ nanoslices is shown in Fig. 2A. 2D sheet-like morphology with sizes varying from 500 nm to several micrometers can be found. Moreover, it can be seen the smooth surface structure. On the contrary, for the hierarchical MoS₂/Bi₂MoO₆ composite, the surfaces of MoS₂ nanoslices were well covered by two-dimensional Bi₂MoO₆ nanoflakes, which are predominantly 10–20 nm in thickness and 100–200 nm in diameter (Fig. 2B). It indicates that Bi₂MoO₆ nanoflakes are gradually grown on MoS₂ nanoslices during the solvothermal reaction via the crystallization, dissolution and recrystallization process similar to our previous reports [18,20,21]. TEM image shown in Fig. 2C further proved that the Bi₂MoO₆ nanoflakes were well dispersed on the surfaces of MoS₂ nanoslices. HRTEM image (Fig. 2D) taken from Fig. 2C clearly displays the resolved lattice fringes of 0.27 nm and 0.305 nm, which corresponds to the (100) of MoS₂ and (111) planes of orthorhombic phase of Bi₂MoO₆, respectively [18,22]. It clearly reveals that MoS₂ and Bi₂MoO₆ have well-mixed heterojunctions in the composite, which can benefit better charge separation and efficient electron transfer within the hybrid



Scheme 1. Schematic illustration of the synthetic procedure of the hierarchical MoS₂/Bi₂MoO₆ composite involving the exfoliation of MoS₂ nanoslices and the in situ growth process of Bi₂MoO₆ nanoflakes on the surface of the exfoliated 2D platform structure of MoS₂ nanoslices.

structure in comparison to pure Bi₂MoO₆. The SEM images of the MoS₂/Bi₂MoO₆ composites with different MoS₂ contents are shown in Fig. S3. When the content of MoS₂ is too low (below 6 wt%), some excess Bi₂MoO₆ nanoflakes detached from the surfaces of MoS₂ nanoslices (Fig. S3A and B). When the content of MoS₂ is high (more than 6 wt%), there are small amount of Bi₂MoO₆ nanoflakes on the surface of MoS₂ nanoslices (Fig. S3D), so sufficient amount of Bi₂MoO₆ should be provided to obtain high coverage of nanoflakes.

To better understand the formation mechanism, the MoS₂/Bi₂MoO₆ composites synthesized from different reaction times were characterized by SEM. As shown in Fig. S1, at the initial reaction stage (0.5 h), it can be found that a thin layer of particulates grow uniformly on the surfaces of exfoliated 2D platform structure of MoS₂ slices. As reaction time extends (2 h), these small crystallites gradually aggregated into relatively large nanoparticles [18]. After a reaction time of 6 h, these nanoparticles gradually dissolved and grew into small nanoslices and further changed into large flake-like structure via the Ostwald Ripening process. The straightforward synthesis strategy for the hierarchical MoS₂/Bi₂MoO₆ composite is schematically depicted in Scheme 1. In the first step, the thick MoS₂ slices were exfoliated to thin 2D platform structure of MoS₂ slices. Then the exfoliated MoS₂ slices were used as substrates to grow Bi₂MoO₆ nanocrystals. The 2D platform structure of MoS₂ determined the surface alignment of the resulting Bi₂MoO₆ nanoflakes. As only one edge of a Bi₂MoO₆ nanoflake is in contact with the 2D MoS₂ substrate, so the growth of the nanoflake in the other direction was confined. Meanwhile, the aggregation of the as-formed Bi₂MoO₆ nanoflakes can be significantly inhibited, and there may form strong interaction between Bi₂MoO₆ and MoS₂.

3.2. Spectra analysis

X-ray photoelectron spectroscopy (XPS) was used to investigate the chemical states of Mo and S in the hierarchical MoS₂/Bi₂MoO₆ composite (6 wt% of MoS₂). Fig. 3A clearly indicates that the product is mainly composed of Mo, Bi, O and S elements (C signals come from the reference sample). Fig. 3B shows the binding energies of Mo 3d_{3/2} and Mo 3d_{5/2} peaks in the Bi₂MoO₆ are located at 235.6 and 232.6 eV, respectively, suggesting that Mo⁶⁺ existed in the

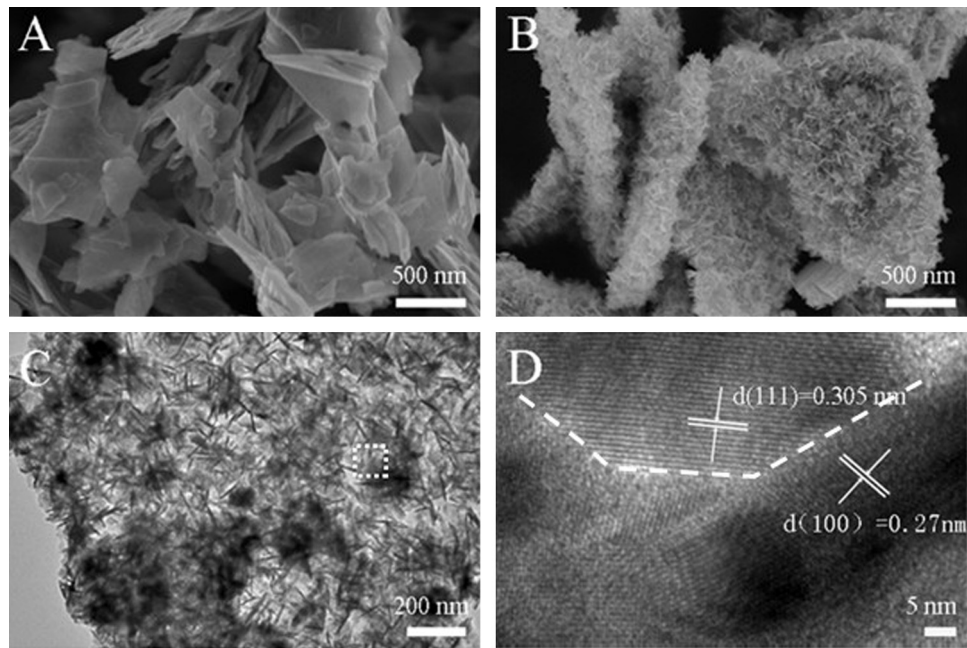


Fig. 2. (A) SEM image of the MoS₂ nanoslices; (B) SEM image of the hierarchical MoS₂/Bi₂MoO₆ composite (6 wt% of MoS₂), (C) low-magnification TEM image of the hierarchical MoS₂/Bi₂MoO₆ composite (6 wt% of MoS₂), (D) HRTEM image of the hierarchical MoS₂/Bi₂MoO₆ composite (6 wt% of MoS₂) in the designated square part in (C).

samples [23]. The binding energies (Fig. 3C) of 159.2 eV for Bi 4f_{7/2} and 164.5 eV for Bi 4f_{5/2} indicate a trivalent oxidation state for bis-bismuth [23]. The peaks corresponding to Bi 4f and Mo 3d in the XPS spectra (Fig. 3B and C) of the hierarchical MoS₂/Bi₂MoO₆ composite slightly shift (about 0.1 eV) toward higher binding energies as compared to pure Bi₂MoO₆ due to the strong interaction between MoS₂

and Bi₂MoO₆. The binding energies of Mo 3d_{3/2} and Mo 3d_{5/2} peaks in the pure MoS₂ are located at 232.5 and 229.3 eV, respectively, suggesting that Mo⁴⁺ existed in the pure MoS₂ [21]. After Bi₂MoO₆ nanoflakes grew on the surface of MoS₂ nanoslices, the corresponding Mo 3d_{3/2} and Mo 3d_{5/2} peaks shifted to 232.8 and 229.7 eV, respectively [24]. Meanwhile, in the hierarchical MoS₂/Bi₂MoO₆

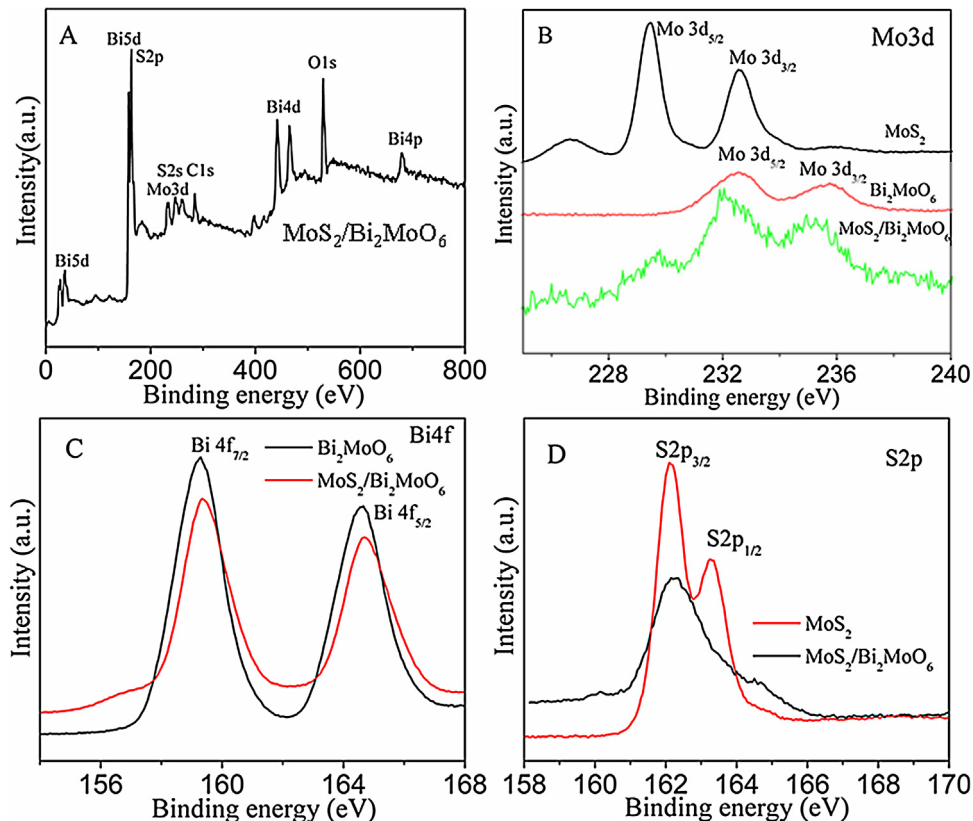


Fig. 3. (A) Survey XPS spectrum of the hierarchical MoS₂/Bi₂MoO₆ composite. High-resolution XPS spectra of Mo 3d (B), Bi 4f (C) and S 2p (D) from Bi₂MoO₆, MoS₂ and the MoS₂/Bi₂MoO₆ composite (6 wt% of MoS₂).

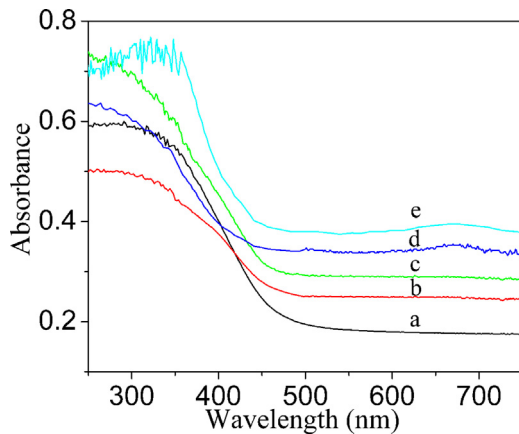


Fig. 4. UV-vis diffuse reflection spectra of Bi_2MoO_6 (a) and the hierarchical $\text{MoS}_2/\text{Bi}_2\text{MoO}_6$ composites with different MoS_2 contents: 2 wt% (b), 4 wt% (c), 6 wt% (d) and 8 wt% (e).

composite, the values of S 2p_{1/2} and S 2p_{3/2} peaks (Fig. 3D) corresponding to MoS_2 are also slightly higher than those of MoS_2 (163.25 and 162.25 eV). The results indicate that there is a strong interaction between Bi_2MoO_6 and MoS_2 in the composite.

A comparison of the UV-vis diffuse reflectance spectra of Bi_2MoO_6 and the $\text{MoS}_2/\text{Bi}_2\text{MoO}_6$ composites with different MoS_2 contents is shown in Fig. 4. Pure Bi_2MoO_6 shows the photoabsorption properties from UV light region to visible light region with the wavelength shorter than 500 nm. Compared with pure Bi_2MoO_6 , there is an enhanced absorbance in the visible-light region (>400 nm) for the $\text{MoS}_2/\text{Bi}_2\text{MoO}_6$ composites. When the content of MoS_2 is relatively high (6 or 8 wt%), there is an additional two absorption peaks located at about 480 and 670 nm, leading to a wide absorption in the visible light region [22]. The corresponding color of the composites also becomes dark gray. The result shows that the addition of MoS_2 nanoslices increases the visible light absorbance [14]. Because of the increased visible light absorbance, a more efficient utilization of the solar energy can be realized. Therefore, it can be inferred that the introduction of MoS_2 nanoslices as the growing substrate of Bi_2MoO_6 nanoflakes is beneficial for the visible-light response of the $\text{MoS}_2/\text{Bi}_2\text{MoO}_6$ composites.

3.3. Charge transfer properties

The surface photovoltaic spectroscopy (SPV) is an effective technique to study the photophysics of excited states generated by photon absorption, and can effectively reflect the information about the process of photoinduced charge separation and transfer in the surface and interface [25]. Fig. 5 shows the SPV spectra of Bi_2MoO_6 and $\text{MoS}_2/\text{Bi}_2\text{MoO}_6$ composites with different MoS_2 contents. The SPV response bands of Bi_2MoO_6 are in the range of 350–550 nm, which is due to the band-band transition (electrons transition from valence band to conduction band) [26]. These hierarchical $\text{MoS}_2/\text{Bi}_2\text{MoO}_6$ composites displayed a similar SPV response to Bi_2MoO_6 , suggesting that the photovoltaic response of the hierarchical $\text{MoS}_2/\text{Bi}_2\text{MoO}_6$ composites mainly resulted from Bi_2MoO_6 . Meanwhile, the photovoltaic response intensities of the hierarchical $\text{MoS}_2/\text{Bi}_2\text{MoO}_6$ composites are significantly higher than that of pure Bi_2MoO_6 . Moreover, with the increase of the MoS_2 contents, the photovoltaic response intensities firstly increased and then decreased. It can be deduced that the junctions formed between Bi_2MoO_6 nanoflakes and MoS_2 nanoslices contributed to the fast injecting of photogenerated electrons from Bi_2MoO_6 nanoflakes into MoS_2 nanoslices and promoted the electron-hole pairs generated in the excited Bi_2MoO_6 efficient separation. When MoS_2 content is too low (less than 6 wt%), there are lots of the

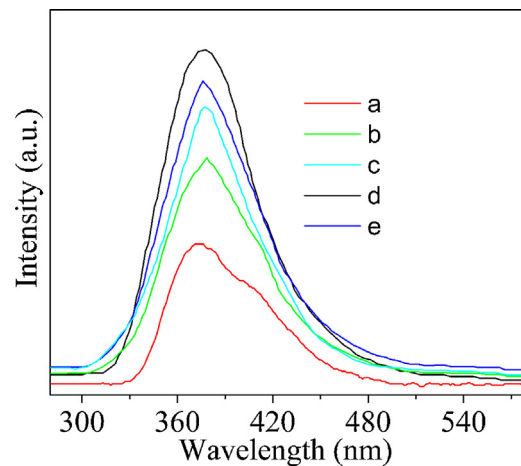


Fig. 5. Surface photovoltaic spectra of Bi_2MoO_6 (a) and the hierarchical $\text{MoS}_2/\text{Bi}_2\text{MoO}_6$ composites with different MoS_2 contents: 2 wt% (b), 4 wt% (c), 6 wt% (d) and 8 wt% (e).

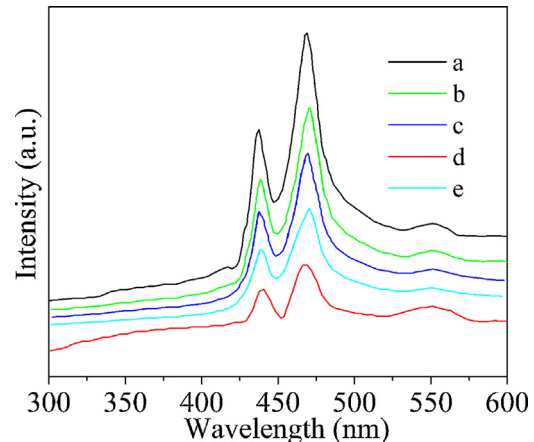


Fig. 6. Photoluminescence spectra of Bi_2MoO_6 (a) and the hierarchical $\text{MoS}_2/\text{Bi}_2\text{MoO}_6$ composites with different MoS_2 contents: 2 wt% (b), 4 wt% (c), 6 wt% (d) and 8 wt% (e).

detached Bi_2MoO_6 , leading to high recombination rate of photoinduced charges and low the photovoltaic response intensity.

Photoluminescence (PL) was used to study the excited state and reveal the differences in the photocatalytic performances of the hierarchical $\text{MoS}_2/\text{Bi}_2\text{MoO}_6$ composites because PL emission arises from the recombination of free carriers [27]. Fig. 6 shows the PL spectra of the as-prepared different samples. It can be seen that, the PL spectra of the hierarchical $\text{MoS}_2/\text{Bi}_2\text{MoO}_6$ composites are similar to that of pure Bi_2MoO_6 . As can be seen, the pure Bi_2MoO_6 has a broad emission peak at around 450 nm, which is attributed to the intrinsic luminescence of Bi_2MoO_6 and is consistent with the UV-visible diffuse reflectance spectra [26]. However, an obvious fluorescence decreases (or quenching) of the hierarchical $\text{MoS}_2/\text{Bi}_2\text{MoO}_6$ composites can be observed compared with that of Bi_2MoO_6 , indicating a much lower recombination rate of photoinduced electrons and holes. The PL results demonstrated that the MoS_2 layers with a two-dimensional π -conjugated structure could serve as an effective electron-accepting material and the formed strong interaction between Bi_2MoO_6 and MoS_2 could improve the separation of electron-hole pairs under visible light irradiation and then electrons easily transfer to MoS_2 sheets, inhibiting a direct recombination of electrons and holes [25]. However, when the MoS_2 content is too low (less than 6 wt%), high recombination

rate of photoinduced electrons and holes caused the fluorescence intensity to increase.

Similar to graphene, both the electron accepting and transporting properties of MoS_2 in the composite would contribute to the effective separation of photogenerated electron–hole pair and a fast interfacial charge transfer, and thereby a higher photocatalytic activity would be achieved [28]. This result can also be varied by the electrochemical impedance technique. Typical electrochemical impedance spectra (EIS) of the pure Bi_2MoO_6 and the hierarchical $\text{MoS}_2/\text{Bi}_2\text{MoO}_6$ composite are presented as Nyquist plots in Fig. S2. For $\text{MoS}_2/\text{Bi}_2\text{MoO}_6$ composite, with the introduction of MoS_2 , though in small amount, the semicircle in the plot became shorter, compared with the pure Bi_2MoO_6 electrodes. This observation indicated that both the solid state interface layer resistance and the charge transfer resistance on the surface of $\text{MoS}_2/\text{Bi}_2\text{MoO}_6$ composite are significantly decreased. The results come from the combination effects. 2D Bi_2MoO_6 nanoflakes and 2D MoS_2 nanoslices can both benefit the charge transfer [29,30]. Meanwhile, in the hierarchical $\text{MoS}_2/\text{Bi}_2\text{MoO}_6$ composite system, the more homogeneous mixture and stronger interaction between two components can accelerate charge transfer and separation. Thus the photocatalytic activity was significantly enhanced.

3.4. Photocatalytic activity

The photocatalytic performances of the hierarchical $\text{MoS}_2/\text{Bi}_2\text{MoO}_6$ composites was compared with those of Bi_2MoO_6 and MoS_2 by photocatalytic dye degradation under visible-light irradiation ($\lambda > 420 \text{ nm}$). RhB was chosen as a representative model pollutant. The establishment of adsorption–desorption equilibrium was obtained under continuous stirring overnight before the degradation reaction was carried out. The temporal evolution of the RhB concentration under visible light irradiation in the presence of different samples is displayed in Fig. 7A. The photolysis of RhB is quite slow under xenon lamp irradiation without photocatalysts. All catalysts are able to degrade RhB, and the photocatalytic activity of the mechanical mixture one (Bi_2MoO_6 and 6 wt% MoS_2) is appreciably higher than that of pure Bi_2MoO_6 , whereas most of the $\text{MoS}_2/\text{Bi}_2\text{MoO}_6$ composites exhibited higher photocatalytic activity than the mechanical mixture one. It suggests that there should be strong interaction between MoS_2 nanoslices and Bi_2MoO_6 nanoflakes in the in situ growth process, which plays an important role in the transfer of photogenerated carriers. When Bi_2MoO_6 nanoflakes are coupled with MoS_2 nanoslices, the Bi_2MoO_6 with 2D nanoflake structure can provide a higher charge carrier mobility throughout the longitudinal direction, so the photo-generated electrons can easily transfer to the MoS_2 moiety, leading to efficient separation and prolonged recombination time of electron–hole pairs, which is confirmed by the results of SPV (Fig. 5), PL (Fig. 6) and EIS measurements (Fig. S2) [31,32]. The existing way of Bi_2MoO_6 nanoflakes oriented on the surface of MoS_2 nanoslices can avoid the excessive aggregation of Bi_2MoO_6 nanoflakes and increase the reaction active sites and reactant adsorption [33]. Meanwhile, the connected nanoflakes act as efficient light scattering units and better capture light. All these factors can speed up the reaction with photogenerated active species ($\text{O}_2^{\bullet-}$ or OH^{\bullet} radicals), which promotes the photocatalytic oxidation process for RhB [34]. Moreover, in our study, there existed strong interaction between MoS_2 and Bi_2MoO_6 , which can facilitate the transfer of photogenerated charge and hence reduce recombination rate of excited carriers. Under visible light irradiation, the photogenerated electrons of Bi_2MoO_6 could transfer easily from the conduction band to MoS_2 nanoslices, so significantly inhibiting the recombination of the photogenerated carriers and improving the photocatalytic ability of samples [35]. Meanwhile, the MoS_2 content has a significant

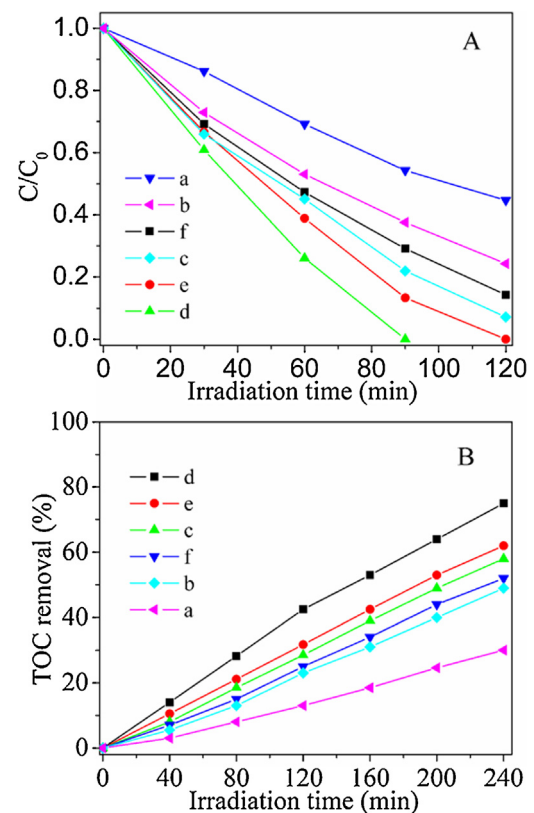


Fig. 7. (A) Comparison of photocatalytic activities and (B) corresponding profiles of total organic carbon (TOC) removals of different catalysts for the degradation of RhB under visible light irradiation, Bi_2MoO_6 (a), hierarchical $\text{MoS}_2/\text{Bi}_2\text{MoO}_6$ composites with different MoS_2 contents: 2 wt% (b), 4 wt% (c), 6 wt% (d), 8 wt% (e), and the mixture of Bi_2MoO_6 and 6 wt% MoS_2 generated by mechanically mixing (f).

influence on the photocatalytic activity of $\text{MoS}_2/\text{Bi}_2\text{MoO}_6$ composites. After introducing only a small amount of MoS_2 , the activity of the 2 wt% $\text{MoS}_2/\text{Bi}_2\text{MoO}_6$ composite is remarkably enhanced. The photocatalytic activity of the composites further increased with increasing MoS_2 content from 2 wt% to 6 wt%. The photocatalytic activity is maximized at the optimal MoS_2 content in the catalyst, and the 6 wt% $\text{MoS}_2/\text{Bi}_2\text{MoO}_6$ composite shows the best catalytic activity, the photodegradation rate of RhB reached 100% when the visible light irradiation time is 80 min, which is 2.2 times higher than that of pure Bi_2MoO_6 (45%, 80 min). When MoS_2 content is higher than 6 wt%, a further increase in MoS_2 content leads to a reduction of the photocatalytic activity. This is partially because that the introduction of a large percentage of dark gray MoS_2 rapidly decreased the intensity of light through the depth of the reaction solution and shielded the Bi_2MoO_6 from absorbing visible light, which resulted in rapid decrease of irradiation passing through the reaction suspension solution [36]. Moreover, excessive MoS_2 in composite indicates low dispersion density of Bi_2MoO_6 nanoflakes on the surface of MoS_2 slices (Fig. S3D). Similarly, excess Bi_2MoO_6 can self-assemble to form aggregates (Fig. S3A,B). Both cases can increase the opportunity for the collision of electrons and holes and promotes the recombination of the photo-generated electron–hole pairs [37].

It has been widely reported that some of the intermediate products in a degradation process are more toxic and carcinogenic than the parent organic compounds. Therefore, the extent of mineralization of RhB in the photocatalytic degradation process was investigated by total organic carbon (TOC) measurement. Fig. 7B displays the temporal evolution of the spectral changes along with the changes of TOC during the photocatalytic

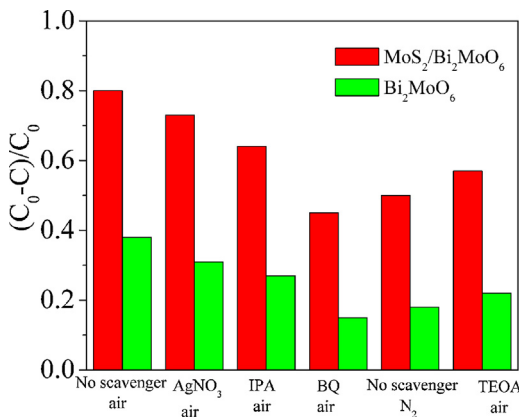


Fig. 8. Comparison of photocatalytic activities of different catalysts with different scavengers during the photocatalytic reaction under 60 min visible light irradiation.

degradation of RhB over the different catalysts. The TOC removal efficiency is about 75%, which confirms that most of the RhB molecules were mineralized by a photocatalytic process. Similar trends of TOC removal and the degradation curves indicated our photodegradation experiments correctly evaluated the photocatalytic activity of the different photocatalysts. Moreover, the reduced TOC contents suggest that the hierarchical MoS₂/Bi₂MoO₆ composites have huge potential in environmental applications such as the mineralization of organic pollutants.

In the photocatalytic oxidation process, the radicals and holes are the main reactive species. Therefore, the trapping experiments of active species during the photocatalytic reaction of the MoS₂/Bi₂MoO₆ composite were done. As shown in Fig. 8, the photocatalytic degradation of RhB was not affected by the addition of 1 mM 2-propanol (IPA, a scavenger of •OH). However, the photocatalytic degradation of RhB decreased obviously when triethanolamine (TEOA, a scavenger of h⁺), benzoquinone (BQ, a scavenger of O₂•⁻) and AgNO₃ (e⁻ scavenger) were added, respectively. Especially in the presence of triethanolamine and benzoquinone. Therefore, it can be concluded that photogenerated holes (h⁺) and O₂•⁻ are the main active species of MoS₂/Bi₂MoO₆ composite for RhB degradation under visible light irradiation [38]. In this system, considering the redox potentials of the conduction band (φ_{CB}) and valence band (φ_{VB}) of the Bi₂MoO₆ at pH 7 is positioned at ca. -0.32 V and +2.34 V vs. NHE, respectively [5,16]. The φ (h⁺) is lower than φ (OH/H₂O) (+2.68 V), and the φ(e⁻) is more negative than φ (O₂/O₂•⁻) (+0.13 V), which can cause the production of O₂•⁻ radicals via the reduction of dissolved O₂ by CB electrons and oxidize a suitable substrate via the excess of valence band holes under visible light irradiation as shown in Fig. S4 [16,38,39]. Meanwhile, the experiment results under the anoxic suspension (nitrogen saturated condition) showed that the photocatalytic activity was obviously decreased, indicating that O₂ acts as an electron trap and the O₂•⁻ is the reactive species. For comparison, the trapping experiment of active species during the photocatalytic reaction of Bi₂MoO₆ was also tested, and both of them had similar photocatalytic mechanism. But the photocatalytic activity of MoS₂/Bi₂MoO₆ composite was significantly enhanced because of the improvement of charge transfer property.

Meanwhile, the degradation process of RhB was also investigated by UV-vis absorption spectra and HPLC chromatograms. As shown in Fig S5A, with the irradiation time prolonged, the intensity of the absorption band of RhB at 554 nm decreased gradually, but no peak shift occurred. This hypsochromic shift of the absorption band was presumed to result from the formation of a series of N-de-ethylated intermediates in a step-wise manner. The result is consistent with the previous work

[40–42]. During the photoreaction, with the visible light irradiating, the intensity of chromatogram peak of RhB (appearing at 16.4 min) decreased continuously. With the quick disappearance of RhB, three intermediates were observed, namely, N,N-diethyl-N'-ethylrhodamine (DER), N-ethyl-N'-ethyl-rhodamine (EER), and N,N-diethyl-rhodamine (DR), appeared at 14, 12.5 and 8.5 min, respectively, which resulted from losing one and/or two ethyl groups from the xanthene ring in the parent RB structure [40,41]. In Fig. S5B, with the quick disappearance of RhB, the intensity of the three peaks of DER, EER and DR species increased slightly and then decreased with further visible irradiation. Therefore, the degradation of RhB was also mainly through the decomposition of the conjugated xanthene. Finally, low molecular weight products were obtained.

One of the practical requirements of photocatalytic materials is chemical stability, and so the stability of the hierarchical MoS₂/Bi₂MoO₆ composite was investigated by RhB recycling the photocatalyst for degradation of RhB. As shown in the Fig. S6, there is only a slight loss of photocatalytic activity after four times consecutive recycling. Moreover, the structure and morphology (Fig. S7) of the hierarchical MoS₂/Bi₂MoO₆ composite also had no change before and after four times consecutive recycling of photoreaction, indicating high stability. The hierarchical MoS₂/Bi₂MoO₆ composite with excellent photocatalytic activity and structure stability provided a probability for the long term degradation of organic contaminants.

4. Conclusions

In summary, the hierarchical MoS₂/Bi₂MoO₆ composites were prepared via a facile solvothermal process using the preexfoliated layered MoS₂ nanoslices as supporting matrix. The prepared hierarchical MoS₂/Bi₂MoO₆ composites showed an enhanced capacity to photocatalytic oxidation of RhB compared with the pure Bi₂MoO₆ due to the efficient separation and transfer across the Bi₂MoO₆ and MoS₂ junction, which is confirmed by the results of SPV, PL and electrochemical impedance measurements. The obtained hierarchical MoS₂/Bi₂MoO₆ composites from this strategy are expected to shed light on structure engineering and design of novel and highly efficient visible-light-driven semiconductor photocatalysts for environmental remediation.

Acknowledgments

We gratefully acknowledge the support of this research by the Key Program Projects of the National Natural Science Foundation of China (no. 21031001), the National Natural Science Foundation of China (51272070, 91122018, 20971040, 21371053), the Cultivation Fund of the Key Scientific and Technical Innovation Project, Ministry of Education of China (no. 708029), Program for Innovative Research Team in University (IRT-1237), Special Research Fund for the Doctoral Program of Higher Education of China (20112301110002), Natural Science Foundation of Heilongjiang Province of China (E201455), Postdoctoral science-research developmental foundation of Heilongjiang province (LBH-Q1136).

Appendix A. Supplementary data

Supplementary data associated with this article can be found, in the online version, at <http://dx.doi.org/10.1016/j.apcatb.2014.08.036>.

References

- [1] D.P. Serrano, J.M. Coronado, Victor A. de la Pena O'Shea, P. Juan, A. Botas, J. Mater. Chem. A 1 (2013) 12016–12027.

[2] F. Fresno, R. Portela, S. Suarez, J.M. Coronado, *J. Mater. Chem. A* 2 (2014) 2863–2884.

[3] Y. Halpin, M.T. Pryce, S. Rau, D. Dinic, J.G. Vos, *Dalton Trans.* 42 (2013) 16243–16254.

[4] J.B. Joo, M. Dahl, N. Li, F. Zaera, Y. Yin, *Energy Environ. Sci.* 6 (2013) 2082–2092.

[5] (a) C. Guo, J. Xu, S. Wang, L. Li, Y. Zhang, X. Li, *CrystEngComm* 14 (2012) 3602–3608; (b) W. Wu, R. Lin, L. Shen, R. Liang, R. Yuan, L. Wu, *RSC Adv.* 3 (2013) 10894–10899.

[6] (a) M. Zhang, J. Xu, R.L. Zong, Y.F. Zhu, *Appl. Catal. B: Environ.* 147 (2014) 229–235; (b) X.R. Li, Y. Dai, Y.D. Ma, S.H. Han, B.B. Huang, *Phys. Chem. Chem. Phys.* 16 (2014) 4230–4235.

[7] Y.D. Hou, A.B. Laursen, J.S. Zhang, G.G. Zhang, Y.S. Zhu, X.C. Wang, S. Dahl, I. Chorkendorff, *Angew. Chem. Int. Ed.* 52 (2013) 3621–3625.

[8] Y.G. Li, H.L. Wang, L.M. Xie, Y.Y. Liang, G.S. Hong, H.J. Dai, *J. Am. Chem. Soc.* 133 (2011) 7296–7299.

[9] (a) S.X. Min, G.X. Lu, *J. Phys. Chem. C* 116 (2012) 25415–25424; (b) Q.J. Xiang, J.G. Yu, M. Jaroniec, *J. Phys. Chem. C* 115 (2011) 7355–7363; (c) S. Dey, H.S.S.R. Matte, S.N. Shirodkar, U.V. Waghmare, C.N.R. Rao, *Chem.—Asian J.* 8 (2013) 1780–1784; (d) F.A. Frame, F.E. Osterloh, *J. Phys. Chem. C* 114 (2010) 10628–10633; (e) M. Wang, G.D. Li, H.Y. Xu, Y.T. Qian, J. Yang, *ACS Appl. Mater. Interfaces* 5 (2013) 1003–1008; (f) X.Y. Zhao, C.W. Hu, M.H. Cao, *Chem.—Asian J.* 8 (2013) 2701–2707; (g) Q.H. Liu, L.Z. Li, Y.F. Li, Z.X. Gao, Z.F. Chen, J. Lu, *J. Phys. Chem. C* 116 (2012) 21556–21562; (h) A.O. Neill, U. Khan, J.N. Coleman, *Chem. Mater.* 24 (2012) 2414–2421; (i) K. Chang, W.X. Chen, *Chem. Commun.* 47 (2011) 4252–4254.

[10] (a) B. Wang, Q. Song, B. Luo, X.L. Li, M.H. Liang, X.L. Feng, M. Wagner, K. Miilten, L.J. Zhi, *Chem.—Asian J.* 8 (2013) 410–413; (b) B. Hinemann, P.G. Moses, J. Bonde, K.P. Jørgensen, J.H. Nielsen, S. Horch, *J. Am. Chem. Soc.* 127 (2005) 5308–5309; (c) U. Maitra, U. Gupta, M. De, R. Datta, A. Govindaraj, C.N.R. Rao, *Angew. Chem. Int. Ed.* 52 (2013) 13057–13061; (d) K.G. Zhou, N.N. Mao, H.X. Wang, Y. Peng, H.L. Zhang, *Angew. Chem. Int. Ed.* 50 (2011) 10839–10842; (e) X. Zong, H. Yan, G. Wu, G. Ma, F. Wen, L. Wang, C. Li, *J. Am. Chem. Soc.* 130 (2008) 7176–7177; (f) Q.J. Xiang, J.G. Yu, M. Jaroniec, *J. Am. Chem. Soc.* 134 (2012) 6575–6578.

[11] X. Huang, Z.Y. Zeng, S.Y. Bao, M.F. Wang, X.Y. Qi, Z.X. Fan, H. Zhang, *Nature Communications*, doi:10.1038/ncomms2472.

[12] (a) J.X. Sun, G. Chen, J.Z. Wu, H.J. Dong, G.H. Xiong, *Appl. Catal. B: Environ.* 132–133 (2013) 304–314; (b) L. Ge, C.C. Han, J. Liu, *Appl. Catal. B: Environ.* 108–109 (2011) 100–107; (c) J.H. Xu, W.Z. Wang, S.M. Sun, L. Wang, *Appl. Catal. B: Environ.* 111–112 (2012) 126–132; (d) S.Y. Dong, Y.R. Cui, Y.F. Wang, Y.K. Li, L.M. Hu, J.Y. Sun, J.H. Sun, *Chem. Eng. J.* 249 (2014) 102–110.

[13] (a) Z. Li, X. Chen, Z. Xue, *CrystEngComm* 15 (2013) 498–508; (b) M. Shang, W. Wang, J. Ren, S. Sun, L. Zhang, *Nanoscale* 3 (2011) 1474–1476; (c) R. Shi, T. Xu, L. Yan, Y. Zhu, J. Zhou, *Catal. Sci. Technol.* 3 (2013) 1757–1764; (d) X. Zhao, Jiuhuiqu, H. Liu, C. Hu, *Environ. Sci. Technol.* 41 (2007) 6802–6807; (e) L. Zhou, M. Yu, J. Yang, Y. Wang, C. Yu, *J. Phys. Chem. C* 114 (2010) 18812–18818; (f) Y. Shimodaira, H. Kato, H. Kobayashi, A. Kudo, *J. Phys. Chem. B* 110 (2006) 17790–17797.

[14] A. Löfberg, G. Sankar, W.V. Beek, E. Bordes-Richard, Rose-Noëlle Vannier, *Cryst. Growth Des.* 12 (2012) 5994–6003.

[15] (a) Y.L. Min, G.Q. He, Q.J. Xu, Y.C. Chen, *J. Mater. Chem. A* 2 (2014) 2578–2584; (b) N. Lu, H.Y. Guo, L. Li, J. Dai, L. Wang, W.N. Mei, X.J. Wu, X.C. Zeng, *Nanoscale* 6 (2014) 2879–2886; (c) Y.S. Xu, Z.J. Zhang, W.D. Zhang, *Dalton Trans.* 43 (2014) 3660–3668; (d) J.L. Wang, H. Feng, K.M. Chen, W.L. Fan, Q. Yang, *Dalton Trans.* 43 (2014) 3990–3998; (e) Z. Wang, J.G. Hou, C. Yang, S.Q. Jiao, H.M. Zhu, *Chem. Commun.* 50 (2014) 1731–1734.

[16] (a) M.Y. Zhang, C.L. Shao, J.B. Mu, Z.Y. Zhang, Z.C. Guo, P. Zhang, Y.C. Liu, *CrysEngComm* 14 (2012) 605–612; (b) M.Y. Zhang, C.L. Shao, J.B. Mu, X.M. Huang, Z.Y. Zhang, Z.C. Guo, P. Zhang, Y.C. Liu, *J. Mater. Chem.* 22 (2012) 577–584; (c) J. Ren, W.Z. Wang, M. Shang, S.M. Sun, E. Gao, *ACS Appl. Mater. Interfaces* 3 (2011) 2529–2533; (d) Y. Zhang, Y.K. Zhu, J.Q. Yu, D.J. Yang, T.W. Ng, P.K. Wong, J.C. Yu, *Nanoscale* 5 (2013) 6307–6310.

[17] K.G. Zhou, N.N. Mao, H.X. Wang, Y. Peng, H.L. Zhang, *Angew. Chem. Int. Ed.* 50 (2011) 10839–10842.

[18] G.H. Tian, Y.J. Chen, W. Zhou, K. Pan, Y.Z. Dong, C.G. Tian, H.G. Fu, *J. Mater. Chem.* 21 (2011) 887–892.

[19] (a) U.K. Sen, S. Mitra, *ACS Appl. Mater. Interfaces* 5 (2013) 1240–1247; (b) Y.G. Li, H.L. Wang, L.M. Xie, Y.Y. Liang, G.S. Hong, H.J. Dai, *J. Am. Chem. Soc.* 133 (2011) 7296–7299; (c) K. Chang, W.X. Chen, *ACS Nano* 5 (2011) 4720–4278.

[20] L.W. Zhang, T.G. Xua, X. Zhao, Y.F. Zhu, *Appl. Catal. B: Environ.* 98 (2010) 138–146.

[21] A.M. Beale, G. Sankar, *Chem. Mater.* 15 (2003) 146–153.

[22] W.J. Zhou, Z.Y. Yin, Y.P. Du, X. Huang, Z.Y. Zeng, Z.X. Fan, H. Liu, J.Y. Wang, H. Zhang, *Small* 9 (2013) 140–147.

[23] J.H. Bi, L. Wu, J. Li, Z.H. Li, X.X. Wang, X.Z. Fu, *Acta Mater.* 55 (2007) 4699–4705.

[24] (a) W. Ho, J.C. Yu, J. Lin, J.G. Yu, P.S. Li, *Langmuir* 20 (2004) 5865–5869; (b) Z.B. Chen, D. Cummins, B.N. Reinecke, E. Clark, M.K. Sunkara, T.F. Jaramillo, *Nano Lett.* 1 (2011) 4168–4175.

[25] (a) Y.H. Lin, D.J. Wang, Q.D. Zhao, M. Yang, Q.L. Zhang, *J. Phys. Chem. B* 108 (2004) 3202–3206; (b) G.H. Tian, L.Q. Jing, C.G. Tian, H.G. Fu, *J. Hazard. Mater.* 161 (2009) 1122–1130.

[26] G.H. Tian, Y.J. Chen, R.T. Zhai, J. Zhou, W. Zhou, R.H. Wang, K. Pan, C.G. Tian, H.G. Fu, *J. Mater. Chem. A* 1 (2013) 6961–6968.

[27] (a) J.G. Yu, T.T. Ma, G. Liu, B. Cheng, *Dalton Trans.* 40 (2011) 6635–6644; (b) J.G. Yu, J.J. Fan, B. Cheng, *J. Power Sources* 196 (2011) 7891–7898.

[28] H. Zhang, X.J. Lv, Y.M. Li, Y. Wang, J.H. Li, *ACS Nano* 4 (2010) 380–386.

[29] Q. Li, B.D. Guo, J.G. Yu, J.R. Ran, B.H. Zhang, H.J. Yan, J.R. Gong, *J. Am. Chem. Soc.* 133 (2011) 10878–10884.

[30] J. Zhang, J.G. Yu, M. Jaroniec, *Nano Lett.* 12 (2012) 4584–4589.

[31] L. Zhao, X.F. Chen, X.C. Wang, Y.J. Zhang, W. Wei, Y.H. Sun, M. Antonietti, M.M. Titirici, *Adv. Mater.* 22 (2010) 3317–3321.

[32] X. Zong, H.J. Yan, G.P. Wu, G.J. Ma, F.Y. Wen, L. Wang, C. Li, *J. Am. Chem. Soc.* 130 (2008) 7176–7177.

[33] J.J. Xu, K. Wang, S.Z. Zu, B.H. Han, Z.X. Wei, *ACS Nano* 4 (2010) 5019–5026.

[34] Y.W. Zhang, J.Q. Tian, H.Y. Li, L. Wang, X.Y. Qin, A.M. Asiri, A.O. Al-Youbi, X.P. Sun, *Langmuir* 28 (2012) 12893–12900.

[35] F.K. Meng, J.T. Li, S.K.C. Shing, M.J. Zhi, N.Q. Wu, *J. Am. Chem. Soc.* 135 (2013) 10286–10289.

[36] (a) Q.J. Xiang, J.G. Yu, M. Jaroniec, *Nanoscale* 3 (2011) 3670–3678; (b) Y.H. Zhang, Z.R. Tang, X.Z. Fu, Y.J. Xu, *ACS Nano* 4 (2010) 7303–7314.

[37] (a) J. Zhou, G.H. Tian, Y.J. Chen, X.Y. Meng, Y.H. Shi, X.R. Cao, K. Pan, H.G. Fu, *Chem. Commun.* 49 (2013) 2237–2239; (b) X.Y. Zhang, H.P. Li, X.L. Cui, Y.H. Lin, *J. Mater. Chem.* 20 (2010) 2801–2806.

[38] L. Ye, J.Y. Liu, Z. Jiang, T.Y. Peng, L. Zan, *Appl. Catal. B: Environ.* 142–143 (2013) 1–7.

[39] Y. Shimodaira, H. Kato, H. Kobayashi, A. Kudo, *J. Phys. Chem. B* 110 (2006) 17790–17797.

[40] X. Hao, Y.F. Zhu, *Environ. Sci. Technol.* 40 (2006) 3367–3372.

[41] P.X. Lei, C.H. Chen, J. Yang, W.H. Ma, J.C. Zhao, L. Zang, *Environ. Sci. Technol.* 39 (2005) 8466–8474.

[42] X.K. Li, J.H. Ye, *J. Phys. Chem. C* 111 (2007) 13109–13116.